Assessment of the Efficacy of MRI for Detection of Changes in Bone Morphology in a Mouse Model of Bone Injury

May A. Taha, BSc,[1] Sarah L. Manske, PhD,[2] Erika Kristensen, BSc,[3] Jaymi T. Taiani, MSc,[4] Roman Krawetz, PhD,[5] Ying Wu, PhD,[1] Dragana Ponjevic, MSc,[6] John R. Matyas, PhD,[6] Steven K. Boyd, PhD,[3,7] Derrick E. Rancourt, PhD,[5] and Jeff F. Dunn, PhD[1,7]*

Purpose: To determine whether magnetic resonance imaging (MRI) could be used to track changes in skeletal morphology during bone healing using high-resolution micro-computed tomography (μCT) as a standard. We used a mouse model of bone injury to compare μCT with MRI.

Materials and Methods: Surgery was performed to induce a burr hole fracture in the mouse tibia. A selection of biomaterials was immediately implanted into the fractures. First we optimized the imaging sequences by testing different MRI pulse sequences. Then changes in bone morphology over the course of fracture repair were assessed using in vivo MRI and μCT. Histology was performed to validate the imaging outcomes.

Results: The rapid acquisition with relaxation enhancement (RARE) sequence provided sufficient contrast between bone and the surrounding tissues to clearly reveal the fracture. It allowed detection of the fracture clearly 1 and 14 days postsurgery and revealed soft tissue changes that were not clear on μCT. In MRI and μCT the fracture was seen at day 1 and partial healing was detected at day 14.

Conclusion: The RARE sequence was the most suitable for MRI bone imaging. It enabled the detection of hard and even soft tissue changes. These findings suggest that MRI could be an effective imaging modality for assessing changes in bone morphology and pathobiology.

Key Words: MRI; μCT; stem cells; bone fracture; spin-echo; animal model

NONINVASIVE IMAGING is needed to study treatment paradigms and to follow outcomes in animal models as well as in patients. Previous studies have demonstrated the potential of tissue engineering-based therapies to promote healing of skeletal injuries, but further animal studies are required to optimize these treatment paradigms (1–5). Micro-computed tomography (μCT) is a well-established tool for assessing bone healing (6). However, the ionizing radiation emitted during μCT imaging becomes hazardous when a research subject or animal needs to have repeated exams (7). By contrast, magnetic resonance imaging (MRI) is based on nonionizing radiation and highlights soft tissues, including bone marrow, periosteum, and surrounding muscles. Moreover, MRI already plays an important clinical role in diagnosing occult fractures, bone contusions, and stress fractures (all of which may not show up on conventional x-rays) (8).

MRI is challenging for studying injuries in bone, especially in very small animal models such as the mouse. This is due to the high resolution required and the susceptibility artifacts generated by the bone–soft tissue interfaces. However, the increased availability of a range of MRI sequences makes it possible to overcome this issue. A goal of this study was to compare MRI sequences to obtain a combination of high-resolution, signal-to-noise (S/N) ratio, contrast

[1]Department of Radiology, Faculty of Medicine, University of Calgary, Calgary, Alberta, Canada.
[2]Biomedical Engineering program, Faculty of Kinesiology, University of Calgary, Calgary, Alberta, Canada.
[3]Department of Mechanical and Manufacturing Engineering, Schulich School of Engineering, University of Calgary, Calgary, Alberta, Canada.
[4]Department of Medical Science, Faculty of Medicine, University of Calgary, Calgary, Alberta, Canada.
[5]Departments of Biochemistry & Molecular Biology, Faculty of Medicine, University of Calgary, Calgary, Alberta, Canada.
[6]Department of Comparative Biology and Experimental Medicine, Faculty of Veterinary Medicine, University of Calgary, Calgary, Alberta, Canada.
[7]McCaig Institute for Bone and Joint Health, University of Calgary, Calgary, Alberta, Canada.

Contract grant sponsor: Canadian Institutes of Health Research (SRMT-CIHR), Alberta Innovates Health Solutions Team in Osteoarthritis.

*Address reprint requests to: J.F.D., Department of Radiology, Faculty of Medicine, University of Calgary, 3330 Hospital Dr., NW, Calgary, Alberta, Canada, T2N 4N1. E-mail: dunnj@ucalgary.ca

between bone and soft tissue, and minimal artifacts in a reasonable acquisition time.

A range of materials have been used in tissue engineering-based bone-healing therapies. Matrigel and Purecol have been used as carriers for stem cells (9). Hydroxyapatite (HA) has been shown to contribute to bone formation by providing an alternative to bone grafts (10). Therefore, we used each of these materials to help determine if they influence image quality. The first goal of this study was to compare MRI sequences in order to obtain a high-resolution image of skeletal tissues with a high S/N ratio, with good contrast between bone and soft tissue, and with minimal artifacts in a reasonable acquisition time. Subsequently, we compared the ability of MRI and μCT to image bone fracture, bone marrow, transplanted biomaterial, and the progress of healing.

MATERIALS AND METHODS

Animal Model

Experiments were approved by the Animal Care Committee and conformed to guidelines established by the Canadian Council on Animal Care. Burr hole fractures were created in 13 female Sv129 mice (Jackson Laboratory, Bar Harbor, ME), 4–6 weeks old. To create the fracture, mice were anesthetized with isoflurane. Mice were given buprenorphine (0.03 mL) and penicillin (0.01 mL) intramuscularly prophylactically as analgesic and antibiotics, respectively. Surgery was performed in a unilateral manner as described by Taiani et al (11). An incision was made along the medial aspect of the tibia. The bone surface was exposed by dissecting the periosteum. Using a sterile dental drill with a 0.5 mm cutting burr, multiple holes were drilled into the tibia ~2 mm apart and to a 1 mm depth across the cortical bone until the opposite cortex was reached (12). The surgical incision was sutured. Animals moved freely in their cages after the surgery.

One animal was used to optimize the imaging sequence parameters. The remaining 12 were used to compare MRI and μCT and were divided into three study groups based on the type of biomaterial used to fill the bone fracture site and the number of holes drilled in the tibia, as described below. Animals were scanned at days 1 and 14 after surgery (groups 1 and 2) or days 1 and 13 after surgery (group 3). Two animals from each group were sacrificed immediately after MRI and tissues removed for histology.

Group 1 ($n = 3$) was used to image the bone fracture filled with embryonic stem cells (ESCs) and biomaterials. Two holes were drilled. The proximal hole was filled ESC-derived osteoblasts in Purecol collagen matrix and the distal hole was left as a control. The ESCs were isolated from male Sv129 mice. Purecol was prepared as a 3D gel using 10 mM beta-glycerol phosphate (BGP). Specifically, 80% v/v 3 mg/mL Purecol solution was mixed with a single ESC suspension (1 million cells/mL) and 20% v/v BGP dissolved in 5× concentrated Dulbecco's modified Eagle's medium (DMEM) (Invitrogen, La Jolla, CA) (13). The produced gel was applied on top of the hole using a scalpel and then tucked into it using a needle tip. The distal hole was left empty. We only drilled two holes in this group in case the stem cells migrated between holes.

Groups 2 and 3 were used to image the injury sites in the presence of biomaterials that are used in conjugation with stem cell therapies. These groups had three holes in each animal, injected with biomaterials and no ESCs. In group 2 ($n = 5$) the proximal hole was not filled (control hole); the middle hole was filled with hydroxyapatite (HA) (BD Biosciences, Canada), and the third hole was injected with Purecol bovine collagen I (3.0 mg/mL, pH 2.0, Advanced Biomatrix, San Diego, USA). The pH of Purecol was adjusted to 7.2. To form the gel the solution was warmed to 37°C (13).

In group 3 ($n = 4$) three holes were drilled. The first two were filled similarly to group 2 (unfilled and HA for holes 1 and 2) while the third hole was filled with Matrigel (100 μL of BD Matrigel in 8–9 mL of DMEM/F-12) using a scalpel and needle tip (hESC-qualified Matrix, BD Biosciences, Canada).

High-Resolution MRI

Hardware

MRI was undertaken using a 9.4T 20 cm horizontal bore Magnex magnet with a Bruker Avance console. A custom-built loop gap resonator (slotted tube solenoid) (1.5 cm length, 0.7 cm internal diameter) was used because it provides a high (S/N) ratio and a uniform magnetic field. This coil is oriented perpendicular to B_0. The body of the mouse was aligned along B_0 and the leg was positioned within the solenoid coils (14,15).

Imaging Sequences

2D images were acquired for three Bruker pulse sequences to determine the optimal MRI sequence and parameters: gradient echo fast low angle shot (FLASH), true fast imaging with steady state precession (True FISP) (16), and spin echo rapid acquisition with relaxation enhancement (RARE) (17) (Table 1). The first two pulse sequences (gradient echo methods) were tested because one can modify the pulse or flip angle and the repetition time (TR) to shorten the acquisition. We used a relatively low flip angle and short TR, which maximized the contrast with a relatively rapid acquisition time. The RARE sequence was tested because spin echo-based images have a relatively reduced susceptibility artifact compared to the gradient echo methods and it has increased S/N ratio compared to a standard spin echo for a given acquisition time. An estimate of optimum parameters was iteratively determined by imaging the same animal with a range of TR/TEs and number of averages. After optimizing the MRI pulse sequence, the RARE proton density weighted (PDW) sequence was selected for imaging of the bone fracture model. The optimum parameters (Table 1 RARE PDW) were used for the next set of experiments (Figs. 2, 3).

Table 1
MRI Parameters of GE-FLASH, True FISP, RARE T_1, and Optimum RARE PDW

Parameter	GE-FLASH	True FISP	RARE T_1	Optimum RARE PDW
FOV	1.28x1.28 cm	2.56 x2.56 cm	1.28 x1.28	1.28x1.28
TR/TE	200/4 ms	4/2 ms	1250/7.6 ms	2000/7.6 ms
NA	12	20	10	12
Matrix	256 x256	128 x128	256 x256	256x256
Slice thickness	0.5 mm	0.5mm	0.5 mm	0.5 mm
Resolution	50x50x500 μm	200x200x500 μm	50x50x500 μm	50x50x500 μm
ETL	NA	NA	4	4
Pulse angle	30°	20°	NA	NA
Acquisition time	10 min. 14 sec	10 min	10 min	19 min

FOV, field of view; TR, repetition time; TE, echo time; NA number of averages; ETL, echo train length, which is the same as RARE factor.

Micro CT

All μCT images were acquired on an in vivo μCT scanner (vivaCT40, Scanco Medical, Brüttisellen, Switzerland). For group 1 the images were acquired with a resolution of 10.0 μm and integration time of 200 msec, while for groups 2 and 3 the resolution was 12.5 μm. The scanning time was 19 minutes.

For 2D visualization we present gray-scale μCT images of a longitudinal section of the bone. For 3D visualization of the bone only, the μCT images were Gaussian filtered (the sigma represents the size of the Gaussian distribution and it was = 1.2 pixels while the support determines the number of neighboring pixels used in the convolution and it was = 1) and segmented so that only voxels with attenuation greater than 25.5% of the maximum gray scale value were included.

Image Alignment

In vivo high-resolution MRI and μCT images were compared visually for the same mouse, at the same timepoint, to contrast both imaging modalities. The comparison was based on the number of visible holes, appearance of bone, bone marrow, surrounding soft tissue, transplanted biomaterial, and the progress of healing.

Histology

Histology was performed at the same timepoints as the imaging. Mice were euthanized using euthanyl (Bimeda-MTC, Cambridge, ON). Tibiae were fixed in 10% NBF (Sigma Aldrich, St. Louis, USA), decalcified with Cal-Ex II (Fisher Scientific, USA) and embedded in paraffin. Hematoxylin and eosin staining was done using 10-μm sections stained with hematoxylin Gills III stain (VWR, Canada) and Harleco eosin Y solution (1% alcohol) (EMD Chemicals, Cherry Hill, NJ). An Olympus microscope was used to acquire the histology images.

RESULTS

MRI Sequence Testing

The burr hole fractures were detected as hypointense areas within the marrow region and as interruptions of the dark line of the cortical bone. They could be readily seen in the RARE image (Fig. 1a). Gradient echo (GE) had higher susceptibility artifacts and hypointense areas surrounding the sites of injuries, making it hard to detect the fractures (Fig. 1b). The True-FISP sequence showed significant artifacts based on field inhomogeneity (Fig. 1c). Although it is acknowledged that additional optimization of True-FISP may improve the image quality, the major susceptibility artifacts associated with the GE methods reduced the value of these images. Therefore, based on qualitative assessment of different MRI sequences used, RARE produced the best contrast between bone and surrounding tissues and the fewest artifacts.

Additionally, we tested different RARE weightings and they all showed the holes in the bone. Images with relatively short TEs (nominally proton density images) provided the highest contrast between bone, bone marrow, and soft tissue (data not shown).

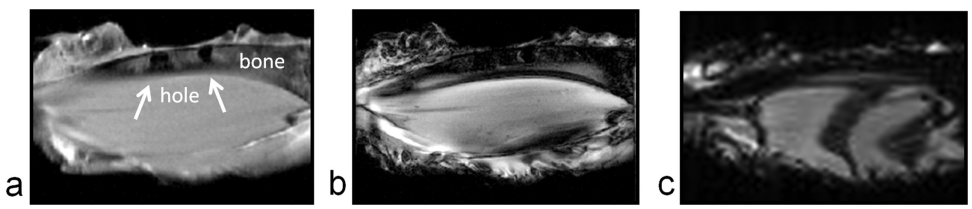

Figure 1. MRI sequence selection. These images were acquired at day 1 postsurgery from the same mouse leg with three MRI sequences: (**a**) RARE T1, (**b**) GE FLASH, and (**c**) True-FISP. For parameters, see Table 1. The foot is to the left and the pelvis to the right. The tibia runs along the top of the image and the gastrocnemius muscle makes up the bulk of the tissue. The increased susceptibility artifacts associated with high-field MRI reduce the quality of the GE and FISP images. The banding in the FISP image could potentially be reduced, but the main point is the lack of capacity to visualize bone. RARE is based on a spin-echo and provides the best quality image for both bone and soft tissue microimaging.

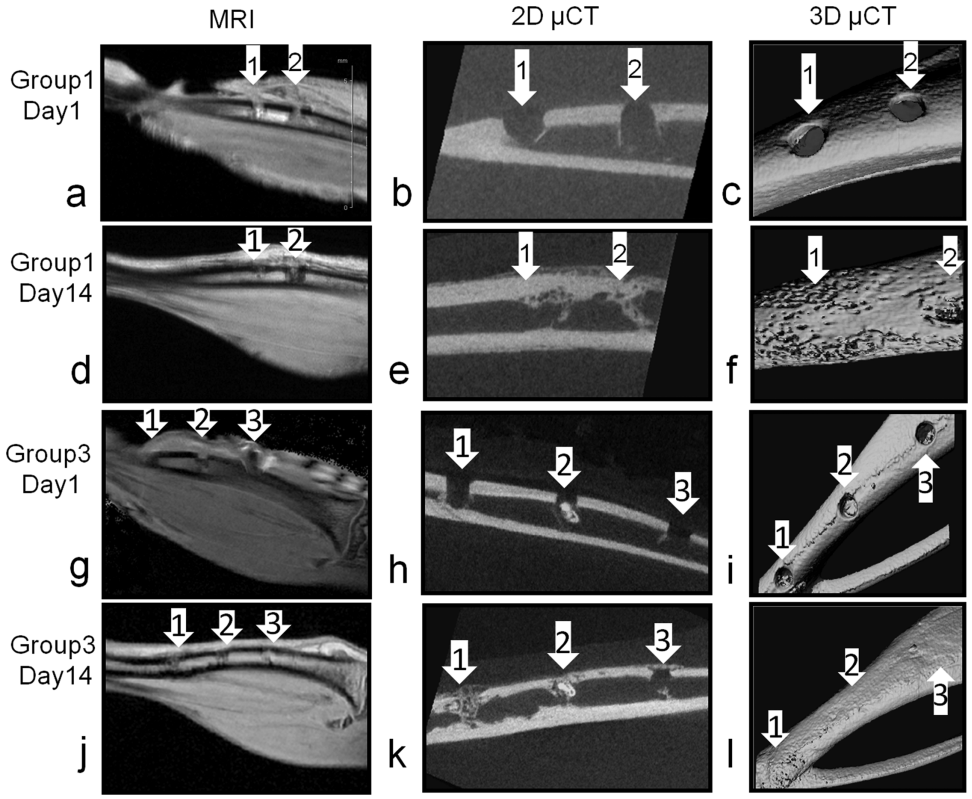

Figure 2. Representative MRI and µCT images from days 1 and 14. In group 1, hole 1 received no treatment, hole 2 received Purecol loaded with ESCs. Row 1 shows the bone at day 1 and row 2 shows the same bone at day 14. At day 1 (**a**) the MR image showed high signal intensity at the site of injury. By day 14 ossification of the callus was observed by both µCT and MRI in the control fracture (hole 1) while the treated fracture (hole 2) showed less recovery of the cortical bone and a larger amount of trabecular bone in the marrow space, suggestive of delayed healing. The MRI image (**d**) clearly shows the difference in signal in the marrow, and the restoration of the black line associated with cortical bone in the hole that is healing faster (hole 1). **g–l**: Mouse images from group 3. Three fractures are visible on days 1 and 14. The fractures had been treated with: 1 = Matrigel, 2 = HA (hydroxyapatite), and 3 = nontreated control. The fractures treated with the biomaterials (holes 1 and 2) showed a different healing pattern than the control fracture (hole 3). The low MRI signal in the marrow of hole 1 (j) corresponds to a hole with significant "trabecular type" growth as seen in the µCT (k). In all the subjects when major differences in healing were observed with µCT, differences could also be seen in MRI. In MRI, it often occurred that not all three holes were visible in one image plane. For this reason, not all holes are visible in (g). We chose this example due to the excellent alignment in (j), showing the different signal intensities associated with the different holes.

Accordingly, RARE relatively weighted to proton density was selected for the remainder of this study (Table 1, RARE PDW).

MRI Longitudinal Study

The muscles, bone marrow, and bone were detectible using MRI. On day 1, 16/17 fractures in all study groups were detected using MRI. One hole was missed in MRI, which could have been due to the curvature of the tibia. Each injury appeared as a gap in the hypointense line corresponding to cortical bone. MRI showed, in all fractures observed, that the injury did not extend through the cortical bone on the opposing side. Control injuries (those without additional implants) had hyperintense spots in the medullary space, and had hyperintensities in the surrounding soft tissue that suggested edema (18) (Fig. 2a,g). In contrast, at day 14 MRI showed continuity of the hypointense line that represents the cortical bone associated with healing. MRI also showed changes in the signal intensity in the medullary space and the surrounding soft tissue with progression of healing (Fig. 2d,j).

µCT Findings

Bone was clearly visible with µCT. Calcified regions, including bone tissue and HA implants, appeared as radiopaque areas. All fractures in all study groups were clearly detected on days 1 and 14. Similar to MRI, µCT imaging verified that the cortical bone opposite to the side of the injury was not breached. At day 1, µCT showed gaps in the cortical bone at the fracture sites and the HA implant was clearly detected in the middle fracture site (Fig. 2h). At day 14 the 2D µCT image showed bridging of the cortical bone at the three holes but with different amount and patterns of trabecular bone in the medullary space. Control holes showed a few bony spicules, while the middle holes showed newly formed bone around the HA implant and profound trabecular bone formation was shown

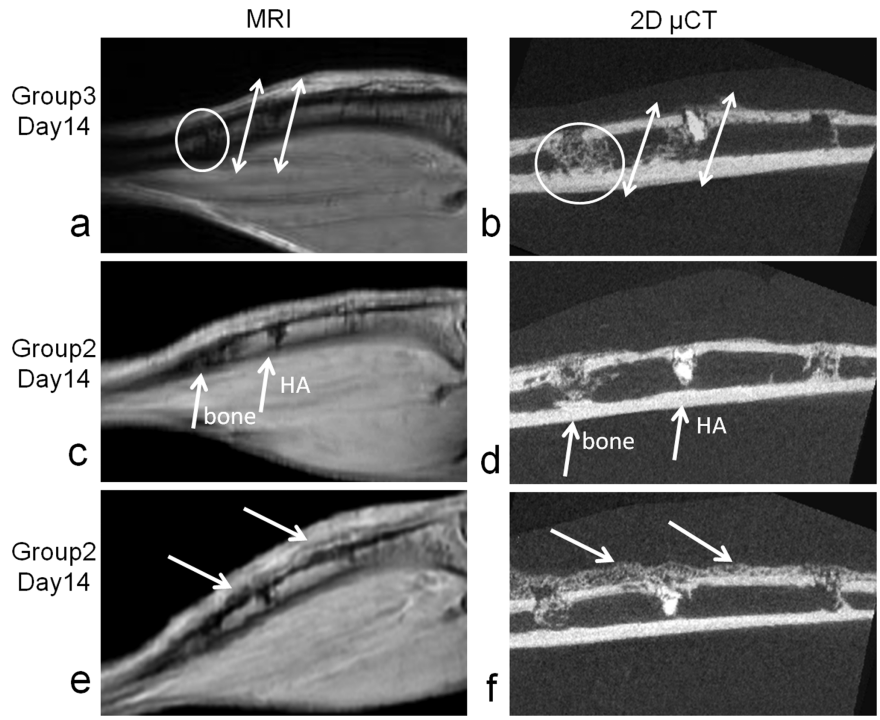

Figure 3. Examples of MRI and µCT correlation at day 14. **a,b**: The pattern of the newly formed trabecular bone shown in the 2D µCT corresponds to regions of intermediate MRI intensity. **c,d**: MRI shows intermediate intensity areas where there is bone, and an even darker hypointense area where there is hydroxyapatite (HA). **e,f**: Extensive ossification over the cortical bone extending beyond the injury sites in one mouse (arrows point to the ossification). This ossification is clearly visible using both MR and µCT. The MRI (e) shows the ossification as a medium intensity region of mottled appearance that exists above the cortical bone and below the skin (arrows).

in the distal hole (Fig. 2k). The 3D µCT was thresholded to the bone only and it showed continuity of the bone surface by day 14 (Fig. 2l).

MRI and µCT Common Findings

At day 14 a thin layer of bone bridging the cortical defect was detected in the fractures using both imaging modalities. Fractures treated with biomaterial implants had trabecular-like bone in their marrow spaces (Fig. 2d,e,j,k).

The fact that MRI and µCT are both sensitive to the presence of trabecular bone is seen in Fig 3. The pattern of the newly formed trabecular bone shown in the µCT corresponded to the intermediate intensity demonstrated in the MR images (Fig. 3a,b). In 2D µCT, the HA appeared more radiopaque than the trabecular-like bone in the distal fracture (Fig. 3d), while in MRI it appeared more hypointense than the trabecular-like bone in the distal fracture (Fig. 3d). Additionally, both imaging modalities detected callus ossification at the defect site in a mouse from group 2 (Fig. 3e,f).

Histology Findings

At day 1, fractures were identified as gaps on one side of the cortical bone with disruption in the bone marrow tissue. In all fractures the presence of a soft tissue reaction composed of a mixture of hematoma, granulation tissue, and the implant material was visualized (Fig. 4a). In the nontreated control fractures, hematoma was predominant (Fig. 4d). In contrast, in the middle fracture (treated with HA), a cavity was detected at the site of the implant where the HA had been dislodged during sectioning, and the defect was surrounded with mostly granulation tissue (Fig. 4c). Where the distal hole was treated with Matrigel (group

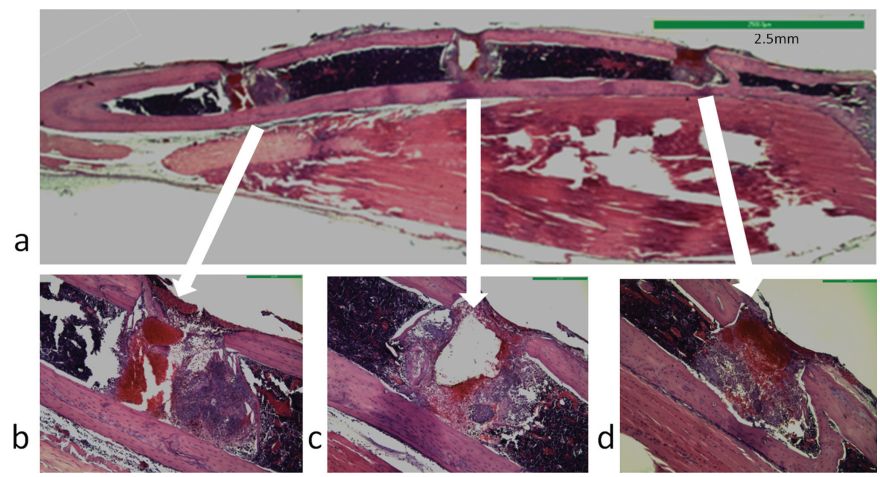

Figure 4. Hematoxylin and eosin-stained sections of a mouse from group 2 at day 1 (**a**). Three fractures are clearly visible, showing a soft tissue reaction composed of a mixture of hematoma and granulation tissue. **b–d**: Higher-power images of each fracture shown in (a): (b) fracture treated with Purecol, (c) fracture treated with HA, and (d) control fracture (nontreated).

3), the gel implant appeared as a white lump. Where the distal hole was treated with Purecol (group 2), the hole was filled largely with a hematoma (Fig. 4b).

At day 14, in group 1 the control holes had apparent amounts of trabecular bone in the medullary space, while in groups 2 and 3 the control holes had the least amount of trabecular bone (data not shown). This suggests that the injury sites can be variable in recovery time-course depending on what material is contained within the injury.

In the middle hole (group 2 and 3) by 14 days, the HA implant was integrated in the newly formed bone which could be correlated with what was seen in the MRI as a dark spot (Figs. 2j, 3a,c,e: middle hole). In the distal hole (with Matrigel and Purecol, depending on the group) greater amounts of trabecular bone were detected in the medullary space compared with the other holes. In group 1, the treated hole (ESCs with Purecol) the gel persisted as a lump in the medullary space. The histology validated the MRI and μCT findings by demonstrating the fracture at day 1 and the remodeling callus at day 14.

DISCUSSION

Of the sequences tested, the RARE pulse sequence provided the best tissue contrast to examine burr hole fractures in a mouse model in a 9.4 T MRI. The high tissue contrast and reduced artifacts provided by the RARE sequence enabled the visualization of the bone injury clearly due to the high distinction between bone, soft tissue, and injury. Moreover, it had a good S/N ratio in a shorter acquisition time (compared to standard spin echo) which is crucial for in vivo studies. These advantages made the RARE sequence superior to the GE and the standard spin echo sequence in imaging the burr hole fracture model.

MRI offered additional information about soft tissue and biomaterial properties during fracture healing compared with μCT. Although MRI did not image bone with as high contrast and resolution as μCT, significant bone detail was observed.

Evidence from the gray-scale images indicates that MRI and μCT showed similar data about the bone response at several stages of healing in response to burr hole fracture.

μCT has been the most common imaging modality for examining bone morphology and microarchitecture in animal models. In the current study, μCT provided higher contrast and resolution of the bones than MRI. However, μCT imaging has some drawbacks, such as exposing the mice to radiation. For repeated measures studies, as for repeated clinical scans, radiation exposure might be hazardous or could induce secondary effects that decrease the efficacy of a therapy (7,19) (ie, cell-based implants may be affected by multiple radiation exposures). μCT also has less contrast than MRI when studying soft tissues such as the medullary space, bone marrow tissue, transplanted biomaterials, and skeletal muscles (20).

The sensitivity of MRI to soft tissues (21) allowed for the detection of edema at day 1 at the site of injury. Edema appeared as hyperintense regions (Fig. 2g), and was validated by the presence of hematoma and granulation tissue at the site of injury in histological sections (Fig. 4).

MRI plays an important clinical role in diagnosing occult fractures, bone contusions, and stress fractures (all of which may not show up on conventional x-rays). Therefore, MRI could be more widely used in the assessment of patients or animal models with bone injuries, especially when serial imaging is needed to avoid unnecessary radiation exposure, or when tissue engineering-based therapies are involved (22).

In this preliminary study we used a small number of mice and high spatial resolution MRI and μCT scanners to obtain images. This was done because following treatment outcome was not the main goal—rather it was to determine if MRI could detect the burr holes and recovery in the holes.

In conclusion, in vivo high-resolution RARE enabled the visualization of the bone fractures in mice due to the high contrast between bone and soft tissue. Therefore, this imaging sequence could be used for assessing bone fracture repair and for evaluating tissue engineering-based therapies in vivo, noninvasively. We also found that MRI can be used as an alternative to μCT to examine the role of various biomaterials in fracture healing, especially when ionizing radiation is contraindicated or when soft tissue and edema are endpoints.

ACKNOWLEDGMENT

We thank Tad Foniak and Dave Kirk for their technical support in MR imaging. We also thank Alison King and Sathya Srinivasan for providing valuable comments.

REFERENCES

1. Miles JD, Weinhold P, Brimmo O, Dahners L. Rat tibial osteotomy model providing a range of normal to impaired healing. J Orthop Res 2010;29:109–115.
2. Aicher WK, Buhring HJ, Hart M, Rolauffs B, Badke A, Klein G. Regeneration of cartilage and bone by defined subsets of mesenchymal stromal cells-Potential and pitfalls. Adv Drug Deliv Rev 2010;63:342–351.
3. Arvidson K, Abdallah BM, Applegate LA, et al. Bone regeneration and stem cells. J Cell Mol Med 2010;15:718–746.
4. Liang H WK, Shimer AL, Li X, Balian G, Shen FH. Use of a bioactive scaffold for the repair of bone defects in a novel reproducible vertebral body defect model. Bone 2010;47:197–204.
5. Swetha M, Sahithi K, Moorthi A, Srinivasan N, Ramasamy K, Selvamurugan N. Biocomposites containing natural polymers and hydroxyapatite for bone tissue engineering. Int J Biol Macromol 2010;47:1–4.
6. Jones AC, Arns CH, Sheppard AP, Hutmacher DW, Milthorpe BK, Knackstedt MA. Assessment of bone ingrowth into porous biomaterials using MICRO-CT. Biomaterials 2007;28:2491–2504.
7. Klinck RJ, Campbell GM, Boyd SK. Radiation effects on bone architecture in mice and rats resulting from in vivo micro-computed tomography scanning. Med Eng Phys 2008;30:888–895.
8. Greenspan A. Orthopedic imaging: a practical approach. 4th ed. Calgary (CA): LWW.
9. Usas A, Ho AM, Cooper GM, Olshanski A, Peng H, Huard J. Bone regeneration mediated by BMP4-expressing muscle-derived stem cells is affected by delivery system. Tissue Eng Part A 2008;15:285–293.

10. Dalkýz M, Özcan A, Yapar M, Gökay N, Yüncü M. Evaluation of the effects of different biomaterials on bone defects. Implant Dent 2000;9:226–235.
11. Taiani JT, Krawetz RJ, Zur Nieden NI, et al. Reduced differentiation efficiency of murine embryonic stem cells in stirred suspension bioreactors. Stem Cells Dev 2010;19:989–998.
12. Uusitalo H, Rantakokko J, Ahonen M, et al. A metaphyseal defect model of the femur for studies of murine bone healing. Bone 2001;28:423–429.
13. Yamashita A, Krawetz R, Rancourt DE. Loss of discordant cells during micro-mass differentiation of embryonic stem cells into the chondrocyte lineage. Cell Death Differ 2009;16:278–286.
14. Martin M, Lemaire C, Tatton WG, Armstrong RL, Struk R. The center-tapped slotted tube autotransformer resonator: a coil for use with a high-resolution small animal imaging system. Magn Reson Med 1988;8:171–179.
15. Benabdallah N, Benahmed N, Benyoucef B, Bouhmidi R, Khelif M. Electromagnetic analysis of the slotted-tube resonator with a circular cross section for MRI applications. Phys Med Biol 2007; 52:4943–4952.
16. Hecht EM, Lee VS, Tanpitukpongse TP, et al. MRI of pelvic floor dysfunction: dynamic true fast imaging with steady-state precession versus HASTE. AJR Am J Roentgenol 2008;191:352–358.
17. Raya JG, Dietrich O, Birkenmaier C, Sommer J, Reiser MF, Baur-Melnyk A. Feasibility of a RARE-based sequence for quantitative diffusion-weighted MRI of the spine. Eur Radiol 2007;17: 2872–2879.
18. Daldrup-Link HE, Henning T, Link TM. MR imaging of therapy-induced changes of bone marrow. Eur Radiol 2007;17:743–761.
19. Green DE, Adler BJ, Chan ME, Rubin CT. Devastation of adult stem cell pools by irradiation precedes collapse of trabecular bone quality and quantity. J Bone Miner Res 2012;27:749–759.
20. Looby S, Flanders A. Spine trauma. Radiol Clin North Am 2011; 49:129–163.
21. Low G, Raby N. Can follow-up radiography for acute scaphoid fracture still be considered a valid investigation? Clin Radiol 2005;60:1106–1110.
22. Warwick R, Willatt JM, Singhal B, Borremans J, Meagher T. Comparison of computed tomographic and magnetic resonance imaging in fracture healing after spinal injury. Spinal Cord 2009;47: 874–877.